An XMM-Newton Early-type Galaxy Atlas

Nazma Islam[1,6,7], Dong-Woo Kim[1], Kenneth Lin[2,3], Ewan O'Sullivan[1], Craig Anderson[1], Giuseppina Fabbiano[1], Jennifer Lauer[1], Douglas Morgan[1], Amy Mossman[1], Alessandro Paggi[4], Ginevra Trinchieri[5], and Saeqa Vrtilek[1]

[1] Center for Astrophysics | Harvard & Smithsonian, 60 Garden Street, Cambridge, MA 02138, USA; nislam@umbc.edu, dkim@cfa.harvard.edu
[2] Department of Astronomy, University of California, Berkeley, CA 94720-3411, USA
[3] Lawrence Berkeley National Laboratory, 1 Cyclotron Road, Berkeley, CA 94720, USA
[4] INAF- Osservatorio Astrofisico di Torino, via Osservatorio 20, I-10025 Pino Torinese, Italy
[5] INAF-Osservatorio Astronomico di Brera, via Brera 28, I-20121 Milano, Italy

Abstract

The distribution of hot interstellar medium in early-type galaxies (ETGs) bears the imprint of the various astrophysical processes it underwent during its evolution. The X-ray observations of these galaxies have identified various structural features related to active galactic nucleus (AGN) and stellar feedback and environmental effects such as merging and sloshing. In our XMM-Newton Galaxy Atlas (NGA) project, we analyze archival observations of 38 ETGs, utilizing the high sensitivity and large field of view of XMM-Newton to construct spatially resolved 2D spectral maps of the hot gas halos. To illustrate our NGA data products in conjunction with the Chandra Galaxy Atlas, we describe two distinct galaxies, NGC 4636 and NGC 1550, in detail. We discuss their evolutionary history with a particular focus on the asymmetric distribution of metal-enriched, low-entropy gas caused by sloshing and AGN-driven uplift. We will release the NGA data products to a dedicated website, from where users can download them to perform further analyses.

Unified Astronomy Thesaurus concepts: Early-type galaxies (429)

1. Introduction

The hot interstellar medium (ISM) in early-type galaxies (ETGs) plays an important role in understanding their formation and evolutionary history. Various astrophysical processes such as active galactic nucleus (AGN) feedback, stellar feedback, and environmental effects such as merging, sloshing, tidal stripping, etc. leave an imprint on the distribution of the hot gas in these ETGs (e.g., see Kim & Pellegrini 2012 and references therein). Although the optical images of these galaxies show a smooth and featureless distribution, the X-ray surface brightness images may reveal the presence of asymmetry in the distribution of the hot gas in these galaxies. Two decades of observations with Chandra and XMM-Newton telescopes have revolutionized our understanding of the distribution of hot gas in ETGs. The unprecedented spatial resolution of Chandra and high sensitivity and large field of view of XMM have allowed us to study in detail the various asymmetric distributions in the hot gas like cold fronts, bubbles, filaments, and X-ray tails, which are indicative of the different astrophysical processes remnant or ongoing in the ETGs.

Previous archival studies on large samples of ETGs focused mainly on the 1D radial profiles and global properties like scaling relations, etc. (O'Sullivan et al. 2003; Diehl & Statler 2007, 2008a, 2008b; Kim & Fabbiano 2013, 2015; Babyk et al. 2018; Lakhchaura et al. 2018; Goulding et al. 2016). As part of the Chandra Early-type Galaxy Atlas project (CGA), Kim et al. (2019, hereafter K19 in the paper) systematically analyzed Chandra observations of 70 E- and S0-type galaxies, with the objective of creating spatially resolved 2D intensity and spectral maps, as well as 1D radial profiles. These 2D spectral maps are important in revealing unique features in the distribution of the hot

gas, which might not be discernible in 1D radial profiles or the 2D surface brightness maps. CGA[8] utilizes robust data analysis pipelines, especially four different spatial binning techniques, to uniformly analyze a large dataset of ETGs.

In this paper, we utilize the large field of view and higher sensitivity of XMM to systematically carry out uniform data analysis of 38 ETGs. The large field of view of XMM-Newton is crucial in studying the diffuse gas emission in the outskirts of the galaxies by measuring their spectral properties and mass profile on a larger scale. This is critical for understanding the interaction of this hot gas with the surrounding medium (e.g., by ram pressure stripping) and neighboring galaxies (e.g., sloshing, merging). The larger effective area of XMM compared to Chandra is also important in studying the metal abundances, especially Fe abundances in the ETGs. Metal abundances in the hot gas of ETGs are the relics of stellar and chemical evolution. They are related to the stellar mass-loss rate and supernova (SN) ejecta, and hence provide important information about the metal enrichment history of the hot gas in ETGs (Ji et al. 2009; Kim et al. 2012; Panagoulia et al. 2015). In this paper, we present Fe abundance maps that were not included in CGA.

The paper is organized in the following order: Section 2 describes the sample selection and the XMM observations. Section 3 describes the data analysis techniques, especially the robust pipelines developed for this project. In Section 4, we describe the results for two galaxies, NGC 4636 and NGC 1550, and their implications for understanding the various astrophysical processes that have affected them. Throughout the paper, the errors are quoted at the 1σ level.

2. Sample Selection and XMM-Newton Observations

Our sample consists of 38 E and S0 galaxies, a sample similar to that used in K19 and for which observations are

---

[6] Present affiliation: Center for Space Science and Technology, University of Maryland, Baltimore County, 1000 Hilltop Circle, Baltimore, MD 21250, USA.
[7] Present affiliation: X-ray Astrophysics Laboratory, NASA Goddard Space Flight Center, Greenbelt, MD 20771, USA.

---

[8] http://cxc.cfa.harvard.edu/GalaxyAtlas/v1/

Table 1
NGA Galaxy List

Name	R.A.	Decl.	D	Type	r_{maj}	r_{min}	PA	Re	$\log(L_K)$	N_H	mid	Eff Exp
I1262	17 33 2.0	+43 45 34.6	130.0	−5.0	0.60	0.32	80.0	0.20	11.42	2.43	90201	24.0
I1459	22 57 10.6	−36 27 44.0	29.2	−5.0	2.62	1.90	42.5	0.62	11.54	1.17	90201	261
I1860	02 49 33.7	−31 11 21.0	93.8	−5.0	0.87	0.60	6.4	0.31	11.57	2.05	90101	69.0
I4296	13 36 39.0	−33 57 57.2	50.8	−5.0	1.69	1.62	45.0	0.80	11.74	4.09	90101	91.0
N0383	01 07 24.9	+32 24 45.0	63.4	−3.0	0.79	0.71	25.0	0.34	11.54	5.41	90201	75.0
N0499	01 23 11.5	+33 27 38.0	54.5	−2.5	0.81	0.64	70.0	0.28	11.31	5.21	90101	85.0
N0507	01 23 40.0	+33 15 20.0	63.8	−2.0	1.55	1.55	60.0	0.69	11.62	5.23	90101	188.0
N0533	01 25 31.4	+01 45 32.8	76.9	−5.0	1.90	1.17	47.5	0.72	11.73	3.07	90201	87.0
N0720	01 53 0.5	−13 44 19.2	27.7	−5.0	2.34	1.20	140.0	0.60	11.31	1.58	90202	216.0
N0741	01 56 21.0	+05 37 44.0	70.9	−5.0	1.48	1.44	90.0	0.64	11.72	4.44	90201	122.0
N1132	02 52 51.8	−01 16 28.8	95.0	−4.5	1.26	0.67	150.0	0.56	11.58	5.19	90101	46.0
N1316	03 22 41.7	−37 12 29.6	21.5	−2.0	6.01	4.26	47.5	1.22	11.76	2.13	90201	266.0
N1332	03 26 17.3	−21 20 7.3	22.9	−3.0	2.34	0.72	112.5	0.46	11.23	2.30	90101	115.0
N1399	03 38 29.1	−35 27 2.7	19.9	−5.0	3.46	3.23	150.0	0.81	11.41	1.49	90201	175.0
N1404	03 38 51.9	−35 35 39.8	21.0	−5.0	1.66	1.48	162.5	0.45	11.25	1.51	90201	311.0
N1407	03 40 11.9	−18 34 48.4	28.8	−5.0	2.29	2.13	60.0	1.06	11.57	5.42	90101	80.0
N1550	04 19 37.9	+02 24 35.7	51.1	−3.2	1.12	0.97	30.0	0.43	11.24	11.25	90301	339.0
N1600	04 31 39.9	−05 05 10.0	57.4	−5.0	1.23	0.83	5.0	0.81	11.63	4.86	90201	139.0
N2300	07 32 20.0	+85 42 34.2	30.4	−2.0	1.41	1.02	108.0	0.55	11.25	5.49	90101	103.0
N3402	10 50 26.1	−12 50 42.3	64.9	−4.0	1.04	1.04	170.0	0.47	11.39	4.50	90101	45.0
N3842	11 44 2.1	+19 56 59.0	97.0	−5.0	0.71	0.51	175.0	0.63	11.67	2.27	90101	48.0
N3923	11 51 1.8	−28 48 22.0	22.9	−5.0	2.94	1.95	47.5	0.88	11.45	6.30	90201	270.0
N4261	12 19 23.2	+05 49 30.8	31.6	−5.0	2.04	1.82	172.5	0.75	11.43	1.58	90201	226.0
N4278	12 20 6.8	+29 16 50.7	16.1	−5.0	2.04	1.90	27.5	0.56	10.87	1.76	90101	57.0
N4325	12 23 6.7	+10 37 16.0	110.0	0.0	0.48	0.32	175.0	0.33	11.29	2.14	90101	41.0
N4374	12 25 3.7	+12 53 13.1	18.4	−5.0	3.23	2.81	122.5	1.02	11.37	2.78	90101	101.0
N4406	12 26 11.7	+12 56 46.0	17.1	−5.0	4.46	2.88	125.0	2.07	11.36	2.69	90101	138.0
N4477	12 30 2.2	+13 38 11.8	16.5	−2.0	1.90	1.73	40.0	0.73	10.83	2.65	90101	27.0
N4552	12 35 39.8	+12 33 22.8	15.3	−5.0	2.56	2.34	150.0	0.68	11.01	2.56	90101	49.0
N4594	12 39 59.4	−11 37 23.0	9.8	1.0	4.35	1.77	87.5	1.19	11.33	3.67	90101	46.0
N4636	12 42 49.9	+02 41 16.0	14.7	−5.0	3.01	2.34	142.5	1.56	11.10	1.82	90101	116.0
N4649	12 43 40.0	+11 33 9.7	16.8	−5.0	3.71	3.01	107.5	1.28	11.49	2.13	90201	240.0
N5044	13 15 24.0	−16 23 7.9	31.2	−5.0	1.48	1.48	10.0	0.42	11.24	4.94	90202	250.0
N5813	15 01 11.3	+01 42 7.1	32.2	−5.0	2.08	1.51	130.0	0.89	11.38	4.25	90301	301.0
N5846	15 06 29.3	+01 36 20.2	24.9	−5.0	2.04	1.90	27.5	0.99	11.34	4.24	90301	346.0
N6338	17 15 23.0	+57 24 40.0	123.0	−2.0	0.76	0.51	15.0	0.48	11.75	2.60	90201	138.0
N6482	17 51 48.8	+23 04 19.0	58.4	−5.0	1.00	0.85	65.0	0.37	11.52	7.77	90301	38.0
N7618	23 19 47.2	+42 51 9.5	74.0	−5.0	0.60	0.50	10.0	0.36	11.46	11.93	90101	39.0
N7619	23 20 14.5	+08 12 22.5	53.0	−5.0	1.26	1.15	40.0	0.57	11.57	5.04	90101	79.0

Note. Column 1: Galaxy name (NGC or IC). Columns 2–3: R.A. and decl. (J2000) from 2MASS via NED (http://ned.ipac.caltech.edu/). Column 4: distance in megaparsecs. Column 5: type taken from the RC3 catalog. Columns 6–7: semimajor and semiminor axis of the D_{25} ellipse in arcminutes taken from the RC3 catalog. Column 8: position angle of the D_{25} ellipse from 2MASS via NED, measured eastward from the north. Column 9: effective radius in arcminutes taken from RC3 catalog. Column 10: K-band luminosity from 2MASS (K_tot mag) via NED (assuming M_K(Sun) = 3.28 mag and D in Column 4). Column 11: Galactic line-of-sight column density of hydrogen in units of 10^{20} cm^{-2}. Column 12: XMM-Newton merge ID (mid–see Table 2 for individual ObsIDs). Column 13: the total (MOS1 + MOS2) effective exposure in kiloseconds after background filtering (see Table 2 for effective exposures of individual ObsIDs).

available from the public XMM archive.[9] XMM carries three X-ray imaging instruments, two EPIC-MOS cameras, and the EPIC-PN cameras. To avoid cross-calibration issues while using these two different types of CCDs and uniformly analyze a large set of observations, we only use observations with MOS cameras (MOS 1 and MOS 2).

Table 1 tabulates the sample of ETGs observed with XMM and analyzed as part of the NGA project, with basic galaxy information (coordinates, distance, galaxy type, size, and K- band luminosities) along with the effective exposures in MOS after removing the background flares. Some of the galaxies have been observed more than once by XMM. We have devised a nomenclature for our sample, merge ID (mid): we assign a five-digit number following the galaxy name, the first digit is 9, followed by mm (where mm is the number of useful observations with XMM; 01 for single observations, 02 for two observations, etc.), and the last two digits (usually "01") are unique serial numbers to separate different combinations of pipeline parameters (e.g., in background flare, point-source detection, source regions).

Table 2 lists the XMM ObsIDs used for each galaxy included in the analysis, the observation dates, the off-axis angle (OAA; in arcmin) of the galaxy center from the telescope aim point, and the effective exposures for each observation after filtering for background flares.

---

[9] https://www.cosmos.esa.int/web/xmm-newton/xsa

Table 2
XMM-Newton Observation Log

Name	mid	ObsID	Obs_Date	OAA	Eff_Exp
I1262	90201	0021140901	2003-01-30	1.03	6.0
		0741580201	2014-11-07	0.26	18.0
I1459	90201	0135980201	2002-04-30	0	57.0
		0760870101	2015-11-02	0	204.0
I1860	90101	0146510401	2003-02-04	0.04	69.0
I4296	90101	0672870101	2011-07-11	2.7	91.0
N0383	90201	0305290101	2005-08-03	0.1	13.0
		0551720101	2008-07-01	0	62.0
N0499	90101	0501280101	2007-08-15	2.29	85.0
N0507	90101	0723800301	2013-07-14	0.03	188.0
N0533	90201	0109860101	2000-12-31	0.46	75.0
		0109860201	2001-01-01	0.46	12.0
N0720	90202	0112300101	2002-07-13	0.15	47.0
		0602010101	2009-12-23	0.04	169.0
N0741	90201	0153030701	2004-01-03	0.68	16.0
		0748190101	2015-01-08	1.73	106.0
N1132	90101	0151490101	2003-07-16	0.03	46.0
N1316	90201	0302780101	2005-08-11	0.05	168.0
		0502070201	2007-08-19	0.05	98.0
N1332	90101	0304190101	2006-01-15	0	115.0
N1399	90201	0012830101	2001-06-27	0.05	12.0
		0400620101	2006-08-23	0.01	163.0
N1404	90201	0304940101	2005-07-30	0	56.0
		0781350101	2016-12-29	0	155.0
N1407	90101	0404750101	2007-02-11	8.67	80.0
N1550	90301	0152150101	2003-02-22	0	45.0
		0723800401	2014-02-02	0.01	117.0
		0723800501	2014-02-06	0.01	177.0
N1600	90201	0400490101	2006-08-14	0.01	32.0
		0400490201	2007-02-06	0.01	107.0
N2300	90101	0022340201	2001-03-16	0.02	103.0
N3402	90101	0146510301	2002-12-20	0.01	45.0
N3842	90101	0602200101	2009-05-27	0.74	48.0
N3923	90201	0027340101	2002-01-03	0.08	73.0
		0602010301	2009-06-23	0.07	197.0
N4261	90201	0056340101	2001-12-16	0.02	56.0
		0502120101	2007-12-16	0.05	170.0
N4278	90101	0205010101	2004-05-23	0.01	57.0
N4325	90101	0108860101	2000-12-24	0.11	41.0
N4374	90101	0673310101	2011-06-01	0.02	101.0
N4406	90101	0108260201	2002-07-01	0.06	138.0
N4472	90301	0761630101	2016-01-05	6.71	190.0
		0761630201	2016-01-07	6.71	177.0
		0761630301	2016-01-09	6.71	174.0
N4552	90101	0141570101	2003-07-10	0.01	49.0
N4594	90101	0084030101	2001-12-28	0.01	46.0
N4636	90101	0111190701	2001-01-05	0.47	116.0
N4649	90201	0021540201	2001-01-02	0.06	96.0
		0502160101	2007-12-19	0.1	144.0
N5044	90202	0037950101	2001-01-12	0.03	42.0
		0554680101	2008-12-27	0.03	208.0
N5813	90301	0302460101	2005-07-23	0.02	58.0
		0554680201	2009-02-11	0.02	122.0
		0554680301	2009-02-17	0.02	121.0
N5846	90301	0021540501	2001-08-26	0.01	29.0
		0723800101	2014-01-21	0.05	149.0
		0723800201	2014-01-17	0.05	168.0
N6338	90201	0741580101	2014-12-04	0.26	24.0
		0792790101	2016-10-12	0.66	114.0
N6482	90301	0304160401	2006-02-18	0	17.0
		0304160501	2006-03-20	0	3.0
		0304160801	2006-04-13	0	18.0
N7618	90101	0302320201	2006-01-20	6.11	39.0
N7619	90101	0149240101	2003-12-16	2.12	79.0

Note. Column 1: galaxy name (NGC or IC). Column 2: merge ID (or mid) is an identification number denoting the number of ObsIDs used for analysis. Column 3: unique XMM-Newton observation ID. Column 4: date of observation. Column 5: off-axis angle (OAA) of the galaxy center in arcminutes. Column 6: effective exposures of individual ObsIDs in kiloseconds after background filtering.

3. Data Analysis

We have developed a robust data analysis pipeline, modeled on the methods developed for the CGA by K19, using SAS threads.[10] Figure 1 shows the flowcharts of the process. The main steps in the data reduction and analysis are

1. Filtering of the MOS event files, removing background flares, applying up-to-date calibration, and tailoring blank files for background estimation (Section 3.1.1).
2. Carrying out source detection on the merged image and removing detected sources to allow clean imaging of the diffuse emission (Section 3.1.2).
3. Adaptively binning with four different binning methods, to determine the optimal spectral extraction regions (Section 3.2).
4. Extracting spectra, fitting them with suitable models, and mapping the spectral parameters (Sections 3.3 and 3.4).

3.1. Reduction of XMM-Newton Data

For a given galaxy, the MOS 1 and MOS 2 data for all the observations are downloaded from the XMM Science Archive (XSA) and processed with SAS version 16.1.0. The SAS tool emchain was used to re-reduce the observations and generate the event files with the latest calibration. The correct blank-sky files, corresponding to the observation mode and filter are also downloaded.[11] For a galaxy having multiple observations, all the observations were reprojected to the tangent plane of the first observation. We first filter the event lists using standard filters for MOS ((PATTERN ⩽ 12) && (PI in [200:12000]) XMMEA_EM).

3.1.1. Background Estimation

The background estimation in XMM is important for extended sources that fill up the entire FOV and therefore do not allow estimation of the local background. The total background emission in XMM/MOS consists of a time-variable or flaring component, mostly particle background and a relatively constant sky background, comprising various components like the cosmic hard X-ray background and soft Galactic emission, and instrumental background components such as fluorescence lines.

To remove the contribution from the flaring particle background, the light curves of MOS 1 and MOS 2 were estimated in 9.5–12 keV energy bands and the time intervals corresponding to count rates greater than 2σ from the average value were excluded. These light curves in a hard energy band were visually inspected to further estimate the times when the background rate is changing gradually throughout the observations or flaring occurs during a significant fraction of an observation. These times were manually removed before re-estimating the good time intervals within 2σ from the average.

The three different methods of background estimation:

1. Simple background subtraction: This method follows from the prescription by Nevalainen et al. (2005), where

---

[10] https://www.cosmos.esa.int/web/xmm-newton/sas-threads
[11] https://xmm-tools.cosmos.esa.int/external/xmm_calibration/background/bs_repository/blanksky_all.html

XMM Archive

MOS 1 and MOS 2

Blank Sky Files

Data reduction,
flare filtering,
reproject
(multiple obsIDs)

flare filter, additional
scaling for 2-10 keV,
reproject

Source detection
(merged images in
0.5-5 keV)

Point sources removed
event files in 0.3-2 keV
and 2-10 keV, per MOS,
per ObsID

Point sources removed
normalised blank sky in
0.3-2 keV and 2-10 keV,
per MOS, per ObsID

Point source
removed
merged images

Adaptive binning
in four methods

Refilling of point
sources removed
regions

Spectral extraction per
region, per obsID, per MOS.
Combine spectra for multiple
obsIDs

Exposure corrected and
smoothed images in
0.5-2.0 keV and 0.5-5.0 keV

Simultaneous fitting of
MOS 1 and MOS 2 with
two component model

Spectral maps of kT,
normalised emission
measure, abundances etc

Imaging Pipeline

Spectral Pipeline

Figure 1. Overview of the data analysis flowchart. The top plot shows the data reduction steps done to the event and blank-sky files. The lower-left plot shows the imaging pipeline, used in constructing the diffuse gas emission images. The lower-right plot shows the spectral pipeline, used in constructing the spectral maps. The details of the various steps in these pipelines are mentioned in detail in Section 3.

the blank-sky files, appropriate to the observation and filter, are used after normalizing the hard energy band count rate to that of the event files.

2. Double background subtraction: This method is proposed by Arnaud et al. (2001) to separate the cosmic X-ray background from the instrumental background by using vignetting-corrected event files. The background spectra are selected from both blank-sky files and a source-free region of the event files. Because the emission from the galaxies in our sample fills up the entire field of view of MOS, this method of background estimation is not applicable in our analysis.

3. Background modeling: This method follows the procedure outlined in "Cookbook for Analysis Procedures for XMM EPIC Observations of Extended Object and the Diffuse Background"[12] (Snowden & Kuntz 2011). The background is partly subtracted and partly modeled in this method, hence it is complex and difficult to implement in the unsupervised fitting procedures developed as part of the pipeline.

Paggi et al. (2017) compared the above three methods of background estimation and found that the results were not heavily dependent on the method of background estimation. Hence we adopted the procedure for background estimation by Nevalainen et al. (2005). We downloaded the appropriate blank-sky files for a given observation and filter[13] (Carter & Read 2007). These blank-sky files were also filtered using good time intervals estimated from their constituent event files. As outlined in Nevalainen et al. (2005), we scaled the count rates in the blank-sky files in 2–10 keV to match the count rates of the event files in 2–10 keV. The count rates of the blank-sky files in 0.3–2 keV were kept unchanged. Although the soft background might be somewhat different, it would not seriously affect our data products in finding hot gas structures in the spectral maps, given that the three different background methods produce consistent results.

3.1.2. Construction of Diffuse Gas Images

For the purpose of detecting the point sources, the MOS 1 and MOS 2 event files, for multiple observations if present, were merged. Nearby galaxies were excluded from this merged image. We ran the CIAO tool wavdetect (with scale = 2, 4, 8, 16 and sigthresh = 10^{-6}), with an appropriate PSF for XMM MOS on the C-band (0.5–5 keV) image. wavdetect might detect false sources near the galaxy center, where the hot gas emission peaks, or sometimes miss the detection of real sources. In such cases, we manually checked the detected point sources and readjusted them. The size of each individual point source was manually checked as well and readjusted as required. We excised the detected point sources to create the point sources removed event files and images in 0.3–10.0 keV, 0.3–2.0 keV, and 2–10 keV, both for observations and blank-sky files. The exposure of the blank-sky files was scaled in 2–10 keV energy band, matching the count rate of source files in 9.5–12 keV. These point-source removed source and scaled blank-sky event files in soft band 0.3–2 keV and hard band 2–10 keV were used for further analysis.

To create the diffuse gas images, we refilled the excised regions of point sources in the point sources removed images with values interpolated from the surrounding pixels using CIAO tools roi, splitroi, and dmfilth. We then generate the exposure-corrected and smoothed point-sourced removed and refilled images with the CIAO tool aconvolve in 0.5–2.0 keV and 0.5–5.0 keV. We note here that merging of different observations was done only to run source detection, create diffuse gas images, and perform adaptive binning (Section 3.2). For the purpose of extracting spectra, we used the point-source removed event and scaled blank-sky files in 0.3–2.0 keV and 2.0–10.0 keV separately for different MOS detectors and different observations.

3.2. Adaptive Binning

We have applied the following four adaptive binning methods, similar to those used in K19, to characterize the 2D spatial and spectral properties of the hot gas in the galaxies.

1. Annulus Binning (AB): In this method, we use circular annuli, where the inner and outer radii of each annulus are adaptively determined based on signal-to-noise ratio (S/N). This method has been widely used to study the 1D radial and spectral profiles of ETGs. The difficulty with this method is that we cannot infer the asymmetry in the distribution of gas in the galaxy because the regions are spherically symmetric.
2. Weighted Voronoi Tessellation Binning (WVT or WB): Originally developed to analyze the optical integral field spectroscopic data by Cappellari & Copin (2003), and later developed for X-ray data by Diehl & Statler (2006), this method provides information on 2D maps of hot gas properties as well as underlying asymmetries in their distribution.
3. Contour Binning (CB): This method is similar to WB, where additionally it groups the areas with similar surface brightness. This utilizes the method developed by Sanders (2006). Similar to WB, this method provides 2D maps of hot gas properties as well as underlying asymmetries in their distributions.
4. Hybrid Binning (HB): This method utilizes the grid-like binning method developed by O'Sullivan et al. (2014). Because this binning method results in overlapping extraction regions, the neighboring bins are not statistically independent. However, it provides complementary information for regions with lower surface brightness with higher spatial resolutions, which is not possible with the other three binning methods.

All the above binning methods are applied to the *C*-band image (0.5–5.0 keV), and the size of the bin is determined by the requirement to achieve $S/N = 50$. While calculating the S/N for all four binning methods, the background counts were considered for estimating the $S/N = src\_counts/(src\_counts + bg\_counts)^{1/2}$.

3.3. Spectral Extraction

After performing the adaptive binning with four methods, we used the SAS tool `evselect` to extract the X-ray spectra for each spatial bin. We use the point-source removed source and blank-sky event files. For each bin, the X-ray spectra were extracted for each MOS detector, each ObsID, in soft (0.3–2.0 keV) and hard (2.0–10.0 keV), using the corresponding source and blank-sky event files. The spectra extracted from the blank-sky event files were scaled to match the count rates of the event files as mentioned in Section 3.1.1. Hence for each spatial bin, two sets of source and background spectral files were extracted, per ObsID, per MOS detector. We generated the response matrices (rmf) and ancillary response matrices (arf) using the SAS tools `rmfgen` and `arfgen`. We combined the spectral and rmf/arf files for different obsids, per bin, with the SAS task `epicspeccombine`. The resulting combined spectra for each MOS and in the soft and hard bands were used in spectral fitting. We also performed a simultaneous fit for the multiple ObsIDs without combining them and found no significant difference in the estimated spectral parameters.

3.4. Spectral Fitting

We carried out joint spectral fits to MOS 1 and MOS 2 spectral files, soft (0.3–2.0 keV) and hard bands (2–10 keV). The spectral fitting was done with `Sherpa`. The spectra were grouped for a minimum of 20 counts to apply χ^2 statistics. We fitted a two-component emission model VAPEC[14] for hot gas (collisionally ionized diffuse gas) and a power law with index 1.7 for undetected low-mass X-ray binaries (Boroson et al. 2011) to the spectral files. We carried out a joint fit to the MOS 1 and MOS 2 spectra and added a constant (cross-normalization between MOS 1 and MOS 2) to the above model. The line-of-sight column density of hydrogen N_H was fixed to the Galactic H I column density (Dickey & Lockman 1990). We fit the emission model VAPEC with two metal abundance ratios: for solar abundances at GRSA (Grevesse & Sauval 1998) and all the metal abundances tied to Fe abundances.

Based on the spectral fits, we produce maps of the various model parameters such as gas temperature (kT), normalized emission measure (normalization of the VAPEC model divided by the area of the bin), abundances, reduced χ^2, etc. We apply a mask at different confidence levels of the spectral parameter (10%, 20%, and 30%) to show only the bins with values of the parameters having errors less than the confidence limit applied. We also produce projected pseudo-entropy ($K_P \sim S_X^{1/3} T$) and projected pseudo-pressure maps ($P_P \sim S_X^{1/2} T$), in arbitrary units, where S_X is the normalized emission measure.

Because the four adaptive binning methods create large numbers of spatial bins, of the order of 10,000 for some galaxies with deep observations, we utilize the Smithsonian Institution High Performance Cluster (SI/HPC).[15] It is a Beowulf cluster consisting of nearly 4000 CPU cores, distributed over 108 computer nodes and 24TB of total RAM. We optimally process the spectral pipeline, including adaptive binning, spectral extraction for all the region files, and spectral fitting and creating maps of temperatures, emission measure, etc., using SI/HPC. An example of the 2D spectral temperature and Fe maps using the contour and WVT binning methods are shown in Figures 3 and 5 for NGC 4636 and NGC 1550.

4. Discussion

Taking advantage of the large effective area and the wide field of view of the XMM-Newton observatory, we use the NGA data products to investigate a number of important scientific questions. For example, the NGA data allow us to trace the full extent of the gas halos of ETGs and study the faint emission from the outskirts of galaxies. This is crucial for studying the interaction of hot gas with its surroundings. Furthermore, the higher S/N spectra obtained with the large effective area make it feasible to investigate the 2D distribution of metal abundances in the hot halos. Along with the temperature map, we construct Fe abundance maps as part of the NGA project. Note that Fe maps were not produced in CGA (K19). The spatial variation of the Fe abundance has direct implications on the metal enrichment (by mass loss of evolved stars and SN explosion) and the transport histories by internal mechanisms (SN-driven winds and AGN-driven buoyant bubbles) and external mechanisms (sloshing and ram pressure

---

[14] https://heasarc.gsfc.nasa.gov/xanadu/xspec/manual/node134.html
[15] https://confluence.si.edu/display/HPC/High+Performance+Computing
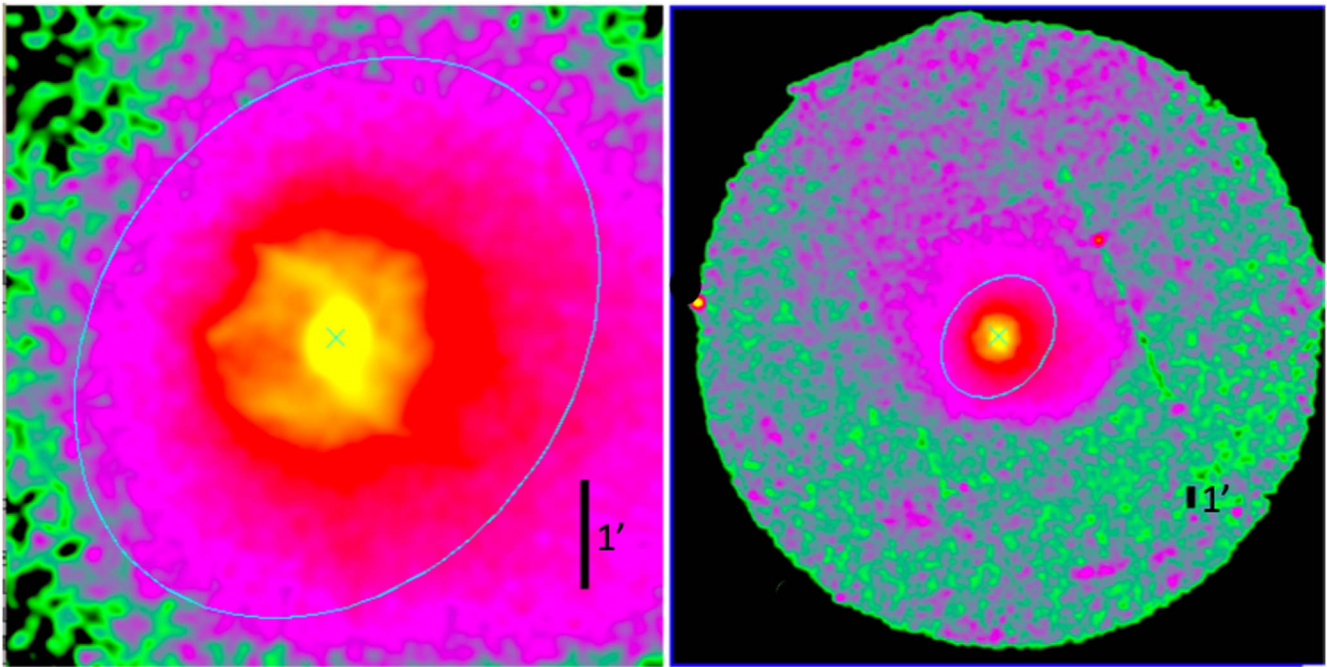
Figure 2. The X-ray surface brightness maps (0.5–2 keV) of NGC 4636 made with the Chandra (left) and XMM (right) observations. The detected point sources were removed and filled with the photons from the surrounding area (see Section 3.1.2), and the exposure correction was applied. The cyan ellipse indicates the D_{25} ellipse (semimajor axis = 3′ or 13 kpc) in both images.

stripping) (e.g., see Kim & Pellegrini 2012). In this paper, we present a few highlights that best demonstrate the XMM-Newton capability by presenting the hot ISM characteristics in two galaxies, NGC 4636 and NGC 1550, with a particular emphasis on the importance of the 2D spectral maps. We will present results using the entire NGA data products in a separate paper.

4.1. NGC 4636

NGC 4636 is an excellent example of small-scale hot gas features, which are related to internal effects, and of a large-scale extended halo, which is related to external effects. This hot gas-rich elliptical galaxy (at $D = 14.7$ Mpc) lies at 10° to the S from the Virgo cluster center and at the northern end of the Virgo South Extension (centered around NGC 4697). The hot halo in this galaxy has been extensively studied using data from various X-ray observatories—Einstein (Forman et al. 1985), ASCA (Awaki et al. 1994), ROSAT (Trinchieri et al. 1994), Chandra (Jones et al. 2002; Johansson et al. 2009), and XMM-Newton (O'Sullivan et al. 2005; Finoguenov et al. 2006; Ahoranta et al. 2016). Previous investigators have produced an intensity map and spectral maps (e.g., Finoguenov et al. 2006 with XMM data; Diehl & Statler 2007 with Chandra data; O'Sullivan et al. 2005 with both data) and in general, we find consistent results. Determining spectral maps (including Fe maps) by multiple binning methods in a uniform manner and examining both Chandra and XMM data help us understand the overall picture of the hot gas evolution.

Figure 2 shows the hot gas distribution of NGC 4636, after point sources were removed and filled, produced with the Chandra (left) and XMM (right) observations. In both panels, we overlay the D_{25} ellipse (cyan) to indicate the stellar system's size and visualize different scales in two images. The Chandra observations reveal that on a small scale (<10 kpc, inside the D_{25} ellipse), two cavities to the NE and SW from the center are

surrounded by the spiral-arms-like features. The smaller-scale features are likely related to nuclear activities and radio jets (e.g., Jones et al. 2002; Giacintucci et al. 2011). Although fine details are not resolved, the XMM observations reveal asymmetrically distributed hot gas—(1) the small-scale (∼10 kpc) elongated structure to the NW–SE direction (similar to the major axis direction of the D25 ellipse, i.e., aligned to the stellar body) inside the D25, (2) the intermediate-scale (∼20 kpc) extension toward the WSW direction beyond the D25 ellipse, and (3) the large-scale (∼50 kpc) extension toward the N direction. The northern extension is faint but pronounced compared to the surface brightness at a similar distance toward the opposite S direction. See also Finoguenov et al. (2006) and their Figure 4. The intermediate-scale and large-scale features (Figure 2 right) are the typical pattern of sloshing (e.g., ZuHone et al. 2018) due to the perturbation by multiple passages of nearby galaxies (see also O'Sullivan et al. 2005; Baldi et al. 2009).

In Figure 3, we show the spectral maps of NGC 4636. The top panels show the T maps made with Chandra (left) and XMM (right) data. The T maps show the asymmetric distribution of the inner cooler gas of ∼0.6 keV, which is elongated to the NW–SE direction inside the D_{25} ellipse, coincident with the small-scale elongation seen in the surface brightness map (Figure 2(b)). The gas temperature at the locations of the two cavities (in the Chandra T map, also seen in Figure 2(a)) is slightly higher (about ∼0.8 keV) than that at the perpendicular direction at a similar distance (∼0.6 keV), as expected by the pressure balance.

Toward the N and E directions from the center, the gas temperature increases with increasing radius and reaches its maximum $kT \sim 1$ keV at $r \sim 15$ kpc (just outside the D_{25} ellipse). To the opposite direction (WSW—indicated by an arrow in Figure 3 top-right), the gas temperature does not increase at the same rate. The intermediate-scale elongation to
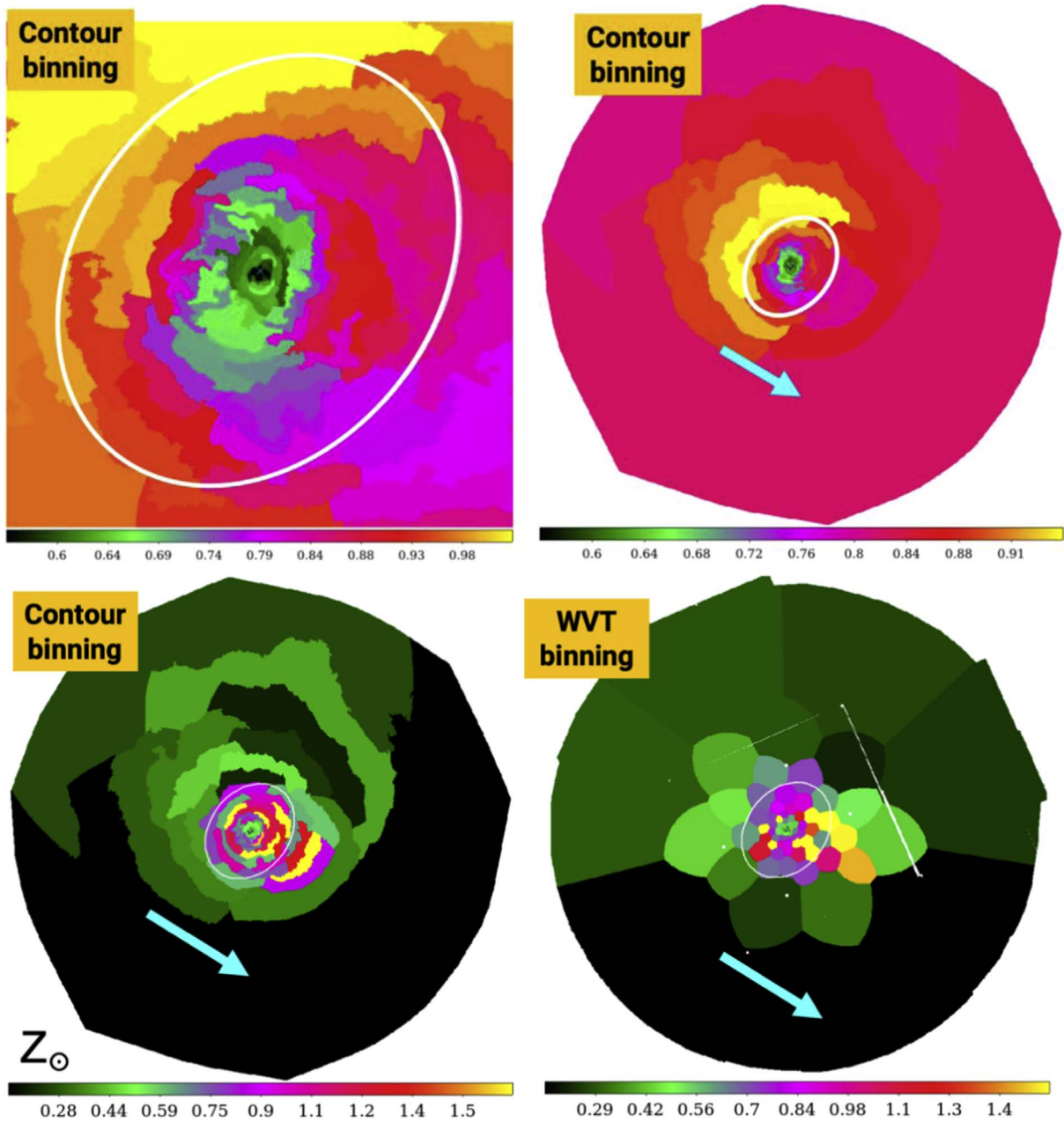
Figure 3. Top panels: the temperature maps of NGC 4636 made with the Chandra (left) and XMM (right) observations. Bottom panels: the Fe abundance maps made with the XMM observations applying the contour binning (left) and the WVT binning (right). The ellipse indicates the D_{25} ellipse (semimajor axis = 3′ or 13 kpc) in all images. The arrow shows the direction of the Fe-rich hot gas.

the WSW direction is cooler ($\sim$0.75 keV) than the gas in the opposite direction (1 keV). On a large scale, the northern extension is slightly cooler ($\sim$0.8 keV) than the opposite side ($\sim$0.9 keV). In summary, the gas in the small-scale elongation (NW–SW), intermediate-scale extension (to WSW), and large-scale enhancement (to N) seen in the surface brightness map (Figure 2 right) is cooler than the gas at a similar distance to the opposite directions.

The Fe map further reveals interesting clues on the nature of the hot gas features. In the bottom panel of Figure 3, we show the Fe map constructed with the XMM observations in two adaptive binning methods (contour binning and WVT as described in Section 3.2). Although the metal abundance and the radial variations in NGC 4636 were previously studied, the 2D Fe maps by multiple binning methods are presented

here for the first time. In the central region ($<$3 kpc; green spatial bins), the Fe abundance is low ($\lesssim$0.5 solar). Apart from this central Fe deficit, which we will discuss below, the hot gas is Fe rich (about solar or higher; red and yellow spatial bins) inside the D_{25} ellipse. Interestingly, the intermediate-scale cooler gas extended to the WSW elongation (seen in the SB map and T map) is richer in Fe ($\sim$1.5 x solar) than the hotter gas in the opposite direction at a similar distance. The large-scale northern extension is Fe rich ($\sim$0.5 solar) compared to the gas at a similar distance to the opposite direction ($\sim$0.2 solar).

In summary, the gas in the intermediate-scale extension to the WSW and the large-scale features (to N) seen in the surface brightness map is cooler and richer in Fe than the gas at a similar distance to the opposite directions. The projected
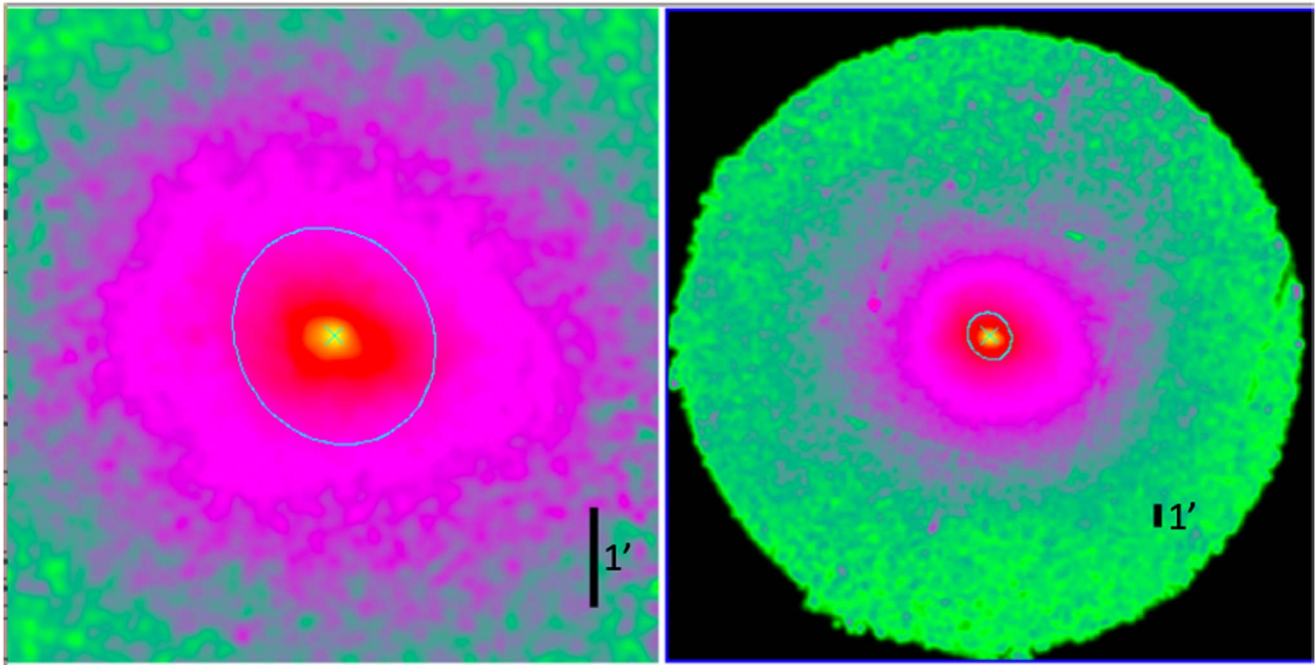
Figure 4. The X-ray surface brightness maps (0.5–2keV) of NGC 1550 made with the Chandra (left) and XMM (right) observations. The detected point sources were removed and filled with the photons from the surrounding area (see Section 3.1.2), and the exposure correction was applied. The cyan ellipse indicates the D_{25} ellipse (semimajor axis = 1′ or 17 kpc) in both images.

pseudo-entropy map ($K_P \sim S_X^{-1/3}$ T) shows the same trend because the dense, low-T gas features have lower entropies (see the NGA web page[16]). We interpret this as an indication that the cooler, metal-enriched, low-entropy gas, originating from the stellar system (inside the D_{25} ellipse) by mass loss and SN ejecta, is stretched out to the WSW on the intermediate scale (20 kpc) and to the N on a large scale (~50 kpc) due to sloshing. The fact that extended gas directions are different with different radii is a typical phenomenon of sloshing as the center of the galaxy has been perturbed, or sloshed, more than once (e.g., see the simulations by ZuHone et al. 2018).

The Fe deficit in the very central region (<3 kpc) in NGC 4636 may require a different physical mechanism. The metallicity deficit at the center was reported in some gas-rich galaxies (e.g., Rasmussen & Ponman 2009; Panagoulia et al. 2015). However, given that the central region is the most complex in thermal and chemical structures of the multiphase hot ISM, this measurement is challenging and may suffer from unknown systematic errors. Even with the two-temperature fit, which was often applied to account for the temperature gradient, the result may still be inconclusive, e.g., because of the limitation of modeling with two components and fixing elements in each component. If the Fe deficit in the center is real, which can be confirmed by a future mission (e.g., XRISM), the possible explanations include resonance scattering, He sedimentation, and stellar and AGN feedback, which may play a role in reducing the observed Fe abundance (see the review in Kim & Pellegrini 2012). Panagoulia et al. (2015) showed that the central deficit is seen more often in the galaxy with an X-ray cavity and a shorter cooling time and suggested that Fe may be incorporated in the central dusty filaments, which are dragged outwards by the bubbling feedback process.

---

16 https://cxc.cfa.harvard.edu/GalaxyAtlas/NGA/v1

4.2. NGC 1550

NGC 1550 is an exciting counterexample to NGC 4636. This group-dominant galaxy (at $D = 51.1$ Mpc) belongs to one of the most X-ray-luminous galaxies within 200 Mpc with $L_{X,GAS} \sim 10^{43}$ erg s^{-1} (Sun et al. 2003). This galaxy has been extensively studied using the Chandra (Sun et al. 2003), XMM (Kawaharada et al. 2009), and Suzaku observations (Sato et al. 2010). Although it does not meet the condition ($\Delta m_{12} > 2$) for a fossil group (Sun et al. 2003), this system is close to a fossil group as a relaxed, merger remnant (Jones et al. 2003; Kawaharada et al. 2009; Sato et al. 2010).

Unlike NGC 4636, the Chandra image (Figure 4 left) indicates that the hot gas in NGC 1550 is relatively smooth, except in the central region where the Chandra image shows an E–W elongation ($r < 10$ kpc; see also Sun et al. 2003; Kolokythas et al. 2020). The XMM observations (Figure 4 right) show that on a large scale (50–100 kpc), the hot halo is smooth and relaxed (see also Figure 3 of Kawaharada et al. 2009). In contrast to NGC 4636, this fossil-like system contains a relaxed hot halo, as expected as an end product of galaxy mergers (e.g., Jones et al. 2000; Khosroshahi et al. 2006). However, the spectral maps (temperature and abundance maps) exhibit interesting features (see below) that are not seen in the SB map and can provide essential clues on the nature of the hot halos.

In Figure 5, we show the spectral maps of NGC 1550. The top panels show the T maps made with Chandra (left) and XMM (right) data. On a small scale (<15 kpc), the 2D temperature map reveals the asymmetric distribution of cooler gas (<1 keV), which is elongated along the E–W direction, more pronounced to the W. Note that this is not aligned with the major axis of the D_{25} ellipse (PA = 30°), i.e., misaligned to the stellar body. On a large scale, the temperature map is smooth, similar to that seen in the SB map. The gas
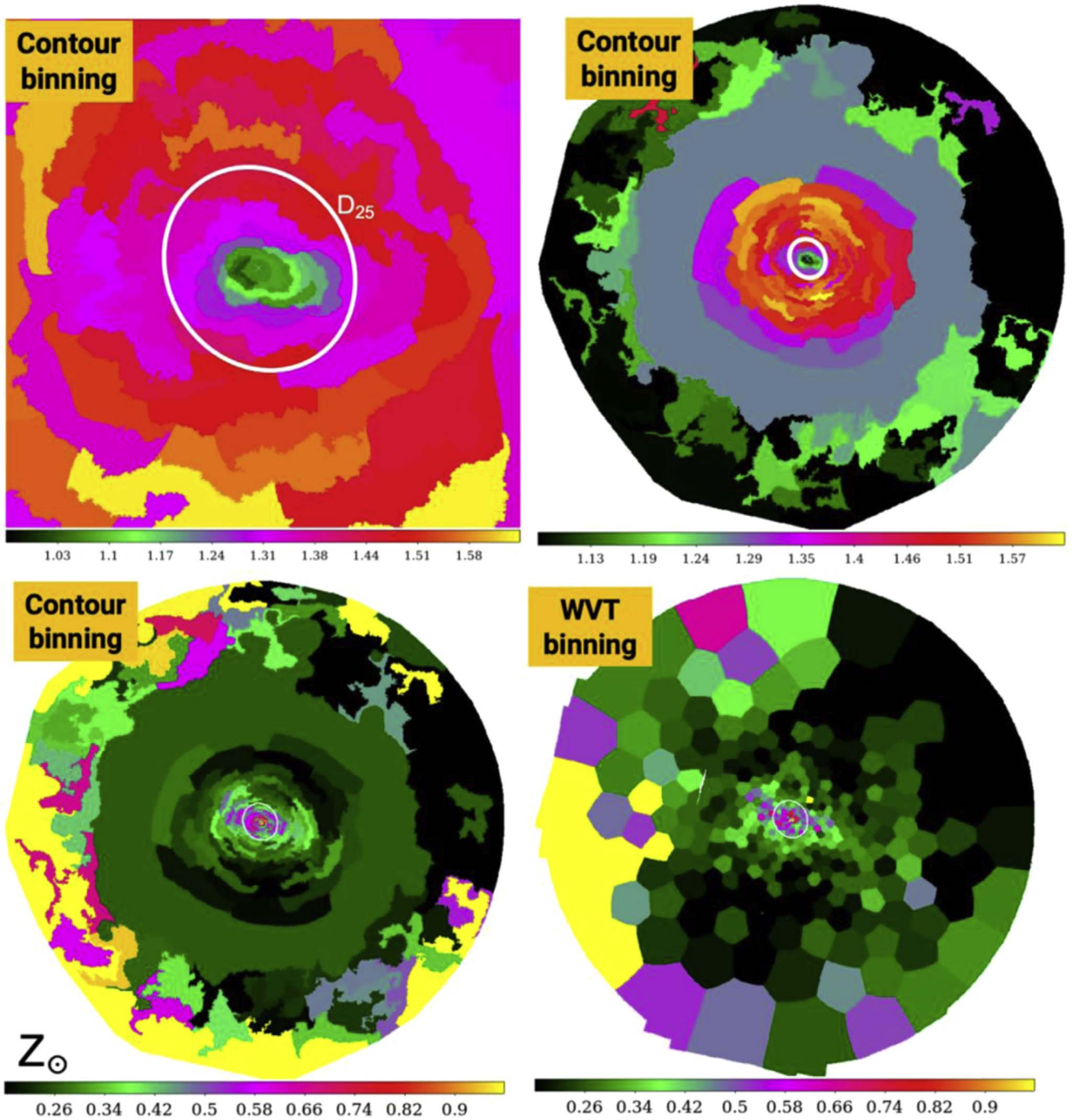
Figure 5. Top panels: the temperature maps of NGC 1550 made with the Chandra (left) and XMM (right) observations. Bottom panels: the Fe abundance maps made with the XMM observations applying the contour binning (left) and the WVT binning (right). The ellipse indicates the D_{25} ellipse (semimajor axis = 1′ or 17 kpc) in all images.

temperature peaks (~1.6 keV) at $r = 30$–50 kpc and slowly declines outward.

The bottom panel of Figure 5 shows the Fe map constructed with the XMM observations in two adaptive binning methods (contour and WVT as described in Section 3.2). Although the metal abundance was previously studied (Sun et al. 2003; Kawaharada et al. 2009; Sato et al. 2010), the 2D Fe map in NGC 1550 is presented here for the first time. The presence of elongated cooler gas is confirmed in the Fe map. The hot gas in the inner E–W elongation is richer in Fe (~0.8× solar) than the gas at a similar distance in other directions (≲0.5 x solar). On a

large scale, the Fe abundance decreases with increasing radius out to $r \sim 100$ kpc. The high Fe abundance near the edge of the FOV is uncertain because of large errors in the Fe measurement, partly because two CCDs (top and bottom of MOS1) were not used in two out of three observations.

Again, we interpret that the cooler, metal-enriched, low-entropy gas, originating from the stellar system (inside the D_{25} ellipse) by mass loss and SN ejecta, is propagating primarily to the EW direction.

It is interesting to note that this E–W extension is aligned with the radio jet-lobe direction. The 1.4 GHz VLA radio
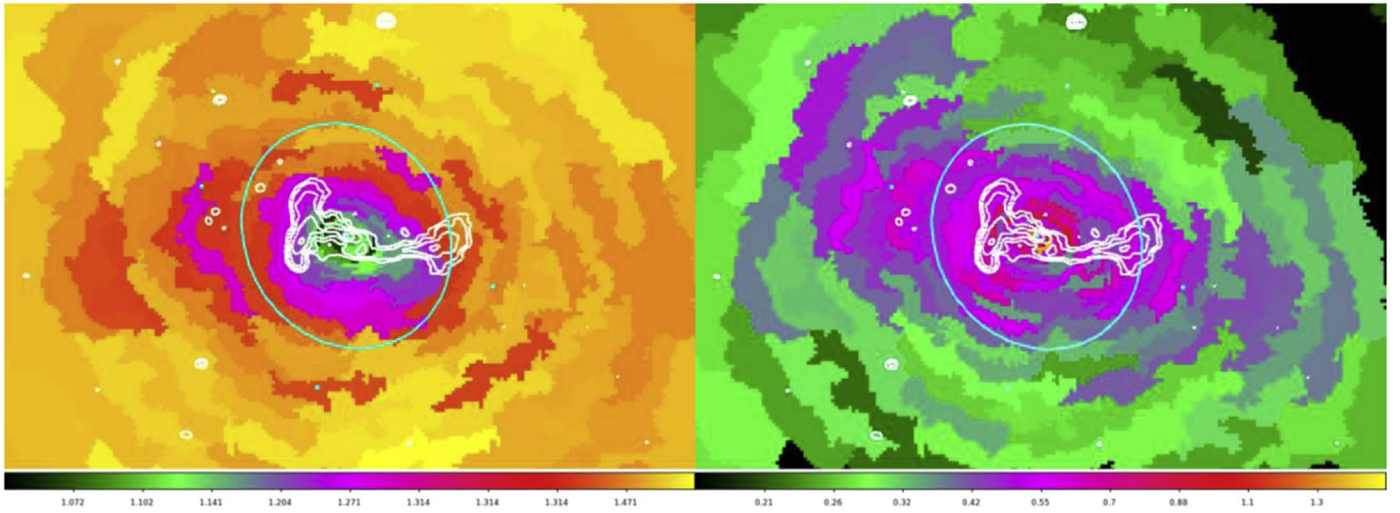
Figure 6. GMRT 610 MHz radio contours (from Kolokythas et al. 2020) showing the AGN jets and lobes overlaid on the T map (left) and the Fe map (right). The cyan ellipse indicates the D_{25} ellipse.

observations of NGC 1550 (Dunn et al. 2010) show two peaks: the primary peak close to the center and the secondary peak at $\sim 45''$ to the W. The 610 and 235 MHz GMRT observations (Kolokythas et al. 2020) further reveal an asymmetric jet-lobe structure, aligned along the E–W direction, with a kink at the W jet and bending at the E jet before flaring up to the lobes on both sides. In Figure 6, the 610 MHz radio contours are overlaid on the T and Fe maps to show the alignment. Kolokythas et al. (2020) examined the association between the radio jet-lobe structure and the asymmetric X-ray surface brightness feature. They considered the ideas of uplift and possible sloshing to explain the X-ray feature.

Here, we further show the apparent association between the T and Fe maps of the hot ISM and the radio structure, particularly to the west, indicating that the elongated cooler, metal-enriched, low-entropy gas is caused by radio lobes, likely by the uplift. The asymmetric Fe distribution, which is aligned with the radio jets and lobes, has previously been seen in a small number of clusters, the best example being Hydra A (Kirkpatrick et al. 2009). See also McNamara et al. (2016) for the theoretical consideration of a possible mechanism of lifting gas via AGN feedback. NGC 1550 represents a nearby, smaller-scale example of Hydra A. Kirkpatrick et al. (2011) have determined the correlation between the jet power and Fe radius ($R_{\mathrm{Fe}} \sim P_{\mathrm{jet}}^{0.42}$) in 10 clusters with asymmetric Fe distributions (see their Figure 3). NGC 1550 roughly follows this relation with $P_{\mathrm{jet}}(\mathrm{west}) \sim$ a few $10^{42}\,\mathrm{erg\,s}^{-1}$ (Kolokythas et al. 2020) and $R_{\mathrm{Fe}} \sim 20\,\mathrm{kpc}$ (to the west) but falls on the lower-left corner in their Figure 3 with the lowest jet power and the smaller Fe radius.

On the contrary, the association of the E radio lode with the extension of the Fe-rich gas is visible only inside the D_{25} ellipse. As seen in Figure 6, the 2D Fe-rich, low-T gas distribution is asymmetric and extending far beyond the E lobe. While the E radio lobe stops at $\sim 10\,\mathrm{kpc}$, the Fe-rich gas reaches roughly twice the D_{25} semimajor axis or at $\sim 40\,\mathrm{kpc}$. Interestingly, this is the location of the possible sloshing front that Kolokythas et al. (2020) identified in the residual image. Given that the extension of low-T, metal-enriched gas is better aligned with the W radio lobe (than the E lobe) and that the E extension of low-T, metal-enriched gas lies far beyond the

radio lobe and reaches the sloshing front (if real), we may be witnessing two mechanisms operating simultaneously—uplifting by the radio lobe to the W and sloshing to the E.

In both NGC 4636 and NGC 1550, the spectral maps reveal that the cooler, metal-enriched, low-entropy gas, originating from the stellar system, is propagating asymmetrically to the large distance from the center, likely due to interactions with the AGN (uplift by radio jet lobe) and with external galaxies (sloshing). To further illustrate the difference between the two galaxies, we compare the radial profiles of their spectral properties.

The radial profile of the hot gas temperature is indicative of various heating mechanisms like AGN feedback (Fabian 2012), stellar feedback (Ciotti et al. 1991), and gravitational heating (Johansson et al. 2009). For galaxy groups and clusters, there is a universal temperature profile, where the temperature is rising rapidly with increasing radius and peaks at $r \sim 0.1\,R_{\mathrm{VIR}}$ (viral radius), and then slowly decreasing at larger radii (Vikhlinin et al. 2005; Sun et al. 2009). A similar trend in the temperature profiles is also seen in ETGs. Kim et al. (2020) studied the radial profiles of 60 ETGs from CGA and propose a "universal" temperature profile of the hot halo in ETGs after considering various observational limitations and selection effects. With the XMM data, we can derive the radial profile of the Fe abundance.

Figure 7 shows the radial profiles of the hot gas properties in NGC 4636 and NGC 1550. The azimuthally averaged quantities were determined with the annulus binning. The other binning methods produce similar results with larger scatters, which reflect the asymmetric distribution of the hot gas (i.e., different values at the same radius), as we described above. In all profiles, the black points are determined with the Fe abundance allowed to vary, and the green points are determined with the Fe abundance fixed at solar. The temperature profiles (left panels) in both galaxies belong to the hybrid-bump type (rising at small radii and falling at large radii), which is typical for a giant elliptical galaxy and the most common (40%) profile among six types of ETGs (Kim et al. 2020).

The Fe abundance profiles (right panels) in these two galaxies are quite different. The Fe abundance in NGC 4636 peaks at $r \sim 5\,\mathrm{kpc}$ and declines both to smaller and larger radii.
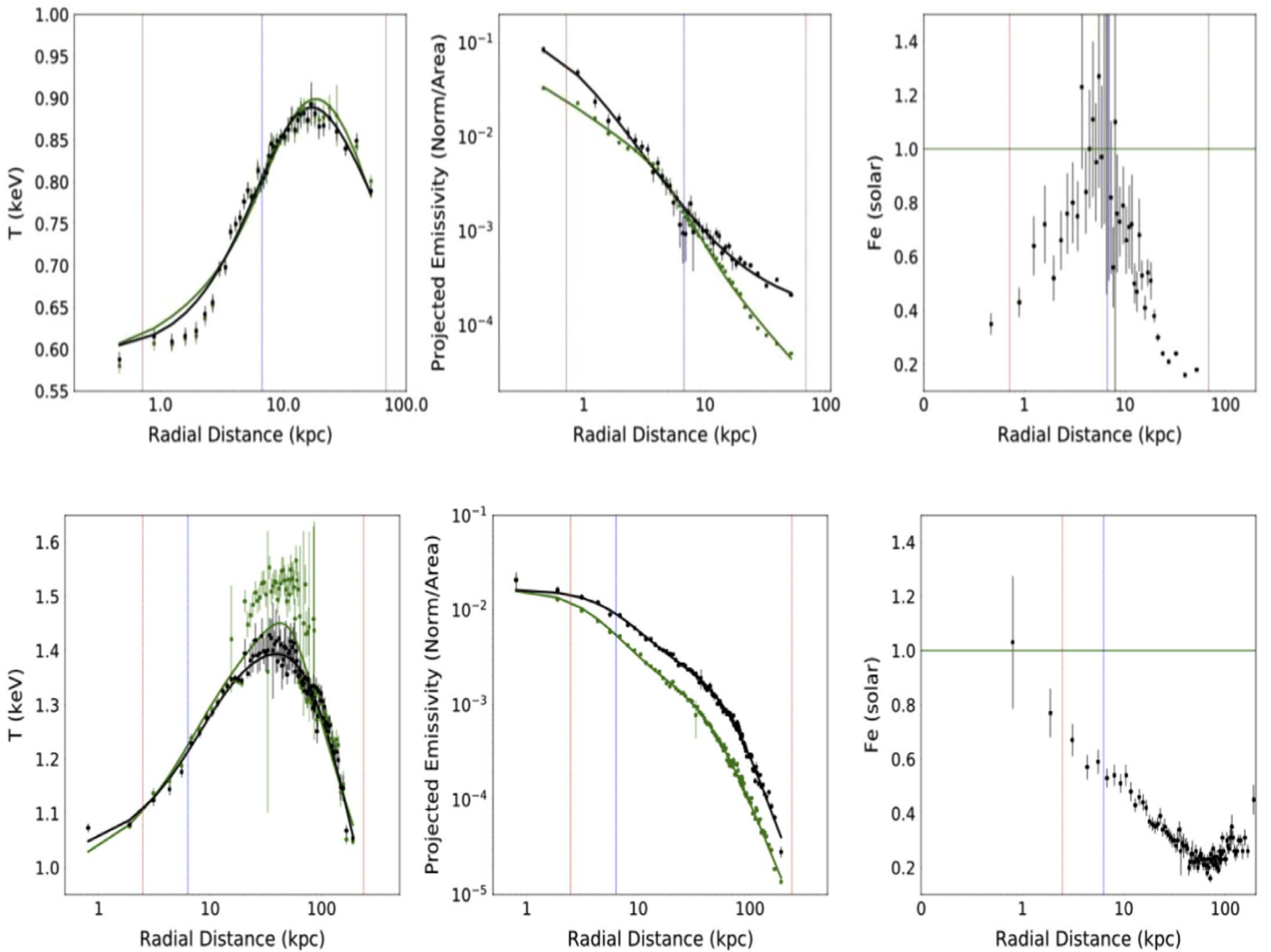
Figure 7. The radial profiles of T (left), projected emissivity (middle), and Fe abundance (right) of the hot gas in (top panel) NGC 4636 and (bottom panel) NGC 1550. The spectral parameters are the azimuthally averaged values determined in the annulus binning. In all profiles, the black points are measured with the Fe abundance allowed to vary, and the green points with the Fe abundance fixed at solar. The blue vertical line denotes the half-light radius, and the dotted red vertical lines are at $r = 10''$ and $16'$, which indicates the inner and outer boundaries set by the XMM PSF and the field of view.

The (peculiar) inward decrease makes the Fe deficit at the center, while the outward decline is expected because Fe is preferentially formed and released from the stars. On the other hand, the Fe abundance in NGC 1550 peaks at the center and monotonically declines with increasing radius. The apparent increase at $r > 100$ kpc is likely unreal because of large systematic/statistical errors.

As described in Kim et al. (2020), the T profiles of ETGs can be classified into six types, with a hybrid-bump type being the most common (43%). The T profiles of NGC 1550 and NGC 4636 belong to this type (the left panel in Figure 7). Because the T profile is closely related to the cooling and heating mechanisms, the proper classification brought new insight into the hot gas thermal history (see Kim et al. 2020). In the same terminology, the Fe profile of NGC 4636 is a hybrid-bump type and that of NGC 1550 is a negative type. The complete classification of Fe profiles, which has not been thoroughly investigated, can allow us to address the chemical enrichment history and metal propagation in relation to the major evolutionary mechanisms, e.g., AGN/stellar feedback and environmental effect, as already seen above. We also note that

the radial variation of the Fe abundance is reflected in the emissivity profile (middle panels)—the emissivity in NGC 4636 increases considerably both inside and outside where the Fe abundance is lower than solar and the emissivity in NGC 1550 increases in all radii except at the center. The variation in emissivity, in turn, affects the density-driven quantities, e.g., pressure and entropy. The full description of the Fe profile and its implication is beyond the scope of this paper. In a forthcoming paper, we will present the Fe profile classification and its related effect on hot gaseous halos.

Our results are generally consistent with previously reported results whenever available. We note that the 2D Fe abundance maps were rarely produced before. However, we have generated an extensive set of data products for each galaxy. Moreover, the spectral maps based on the four different spatial binning methods are complementary with each other. For example, AB shows the radial profiles, WB and CB show the statistically substantial quantities with associated errors, and HB can pick up small-scale features. As shown in our two test cases (NGC 1550 and NGC 4636), with the NGA data products, we can address a complete picture in conjunction

with the CGA products, including fine details and large-scale extended features.

5. Summary

We have developed robust pipelines to uniformly analyze the XMM data. Taking advantage of the high sensitivity and large field of view of the XMM, we have produced 2D spectral maps (e.g., temperature, emission measure, and Fe abundance) of hot gaseous halos in 38 early-type galaxies and made the data products publicly available at the dedicated website.[17]

Our data products are most valuable to investigate the large-scale features of hot gaseous halos in ETGs and the distribution of metal enrichment throughout the galaxies, particularly when used in conjunction with the Chandra Galaxy Atlas (K19), which is optimal for examining the central region at high spatial resolution. To illustrate the data quality and application, we describe two distinct galaxies—NGC 4636 and NGC 1550 —in detail. The spectral maps reveal that in both galaxies, the low-temperature, metal-enriched, low-entropy gas is propagating asymmetrically to large distances from the center, due to the internal (uplift by radio jet-lobe) and external (sloshing by nearby galaxies) mechanisms. In particular, it is interesting to note that both mechanisms are probably taking place in NGC 1550. The Fe radial profiles of the two galaxies are quite different (hybrid bump in NGC 4636 and negative in NGC 1550), indicating that the Fe profile varies from one galaxy to another and could affect density-driven quantities of hot halos. We plan to address the full detail of the Fe profiles and the related implications in a separate paper.
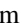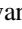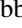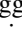
Appendix
NGA Data Products

A quick look of the optical image, diffuse X-ray gas images in different energy bands, temperature, emission measure, pseudo-pressure, pseudo-entropy, and Fe abundance maps constructed with the four binning methods is available on the NGA website. The following downloadable data products are made available there as well. They include FITS files and ds9 PNG figures, which can be used for further analyses and directly compared with other wavelength data. The spectral maps (24 or 28) per (4) binning method per (6 or 7) spectral parameter are stored in two subfolders, one for fixed Fe and another for variable Fe. Because the number of spatial bins is large, the extracted source and background spectra along with its rmfs/arfs are not included in the data release. However, the FITS file "binno.fits" can be used to identify the bin number of the region of interest, and the ASCII file "sum_rad.dat" contains a summary of fitting results.

1. ${gmv}_evt.fits.gz—a merged event file which combined-s all ObsIDs and both MOS1 and MOS2. ${gmv} indicate galaxy name, merge id (mid), and version. ${gmv} looks like N4636_90101_v01.
2. ${gmv}_{e}_img.fits—a combined image file. ${e} is the energy band used, G 0.5–2.0 keV and C 0.5–5 keV.
3. ${gmv}_{e}_exp.fits—a combined exposure map.
4. ${gmv}_{e}_diff_img.fits—a diffuse image file after subtracting and filling detected point sources.
5. ${gmv}_{e}_sm_diff_flux.fits—an exposure-corrected, smoothed, diffuse image file.
6. ${gmv}_{e}_sm_diff_flux.png—same, but a ds9 PNG file
7. ${gmv}_src_psfsize.fits—a FITS list of detected sources
8. ${gmv}_OX.png—a PNG file with an optical DSS image and a raw X-ray image side by side.
9. ${gmv}_rgb.png—a false (three) color image. The energy bands used in RGB are 0.5–1.2, 1.2–2, and 2–7 keV, respectively.
10. ${gm}_{xB}_{Smap}.fits—a FITS image per binning method and per spectral parameter. xB indicates a binning method (AB, WB, CB, or HB). Smap indicates a spectral map (Imap for intensity, Tmap for temperature, Cmap for χ^2, N for normalization/area or EM, P for pressure, K for entropy, or Fe for Fe abundance).
11. ${gm}_{xB}_{Smap}.png—the same, but a ds9 PNG file.
12. ${gm}_{xB}_sum_rad.dat—an ASCII table containing (1) bin number, (2) galactocentric distance in arcminutes determined by photon-weighted mean distance from the galaxy center, (3) area of the bin in pixels (one pixel is 2″ x 2″) (4–5) total and net counts, (6) reduced χ^2, (7–9) best-fit T and its 1σ lower and upper bounds, (10) T error in percent, (11–13) APEC normalization parameter divided by bin area and its 1 lower and upper bounds, and (14–16) best-fit Fe abundance and its 1 lower and upper bounds.
13. ${gm}_{xB}_binno.fits—a FITS image file with pixel value = bin number.

ORCID iDs

Nazma Islam ● https://orcid.org/0000-0002-2413-9301
Dong-Woo Kim ● https://orcid.org/0000-0002-7386-944X
Ewan O'Sullivan ● https://orcid.org/0000-0002-5671-6900
Giuseppina Fabbiano ● https://orcid.org/0000-0002-3554-3318
Alessandro Paggi ● https://orcid.org/0000-0002-5646-2410
Ginevra Trinchieri ● https://orcid.org/0000-0002-0227-502X
Saeqa Vrtilek ● https://orcid.org/0000-0002-7521-9897

References

Ahoranta, J., Finoguenov, A., Pinto, C., et al. 2016, A&A, 592, A145
Arnaud, M., Neumann, D. M., Aghanim, N., et al. 2001, A&A, 365, L80
Awaki, H., Mushotzky, R., Tsuru, T., et al. 1994, PASJ, 46, L65
Babyk, I. V., McNamara, B. R., Nulsen, P. E. J., et al. 2018, ApJ, 857, 32
Baldi, A., Forman, W., Jones, C., et al. 2009, ApJ, 707, 1034
Boroson, B., Kim, D.-W., & Fabbiano, G. 2011, ApJ, 729, 12
Cappellari, M., & Copin, Y. 2003, MNRAS, 342, 345
Carter, J. A., & Read, A. M. 2007, A&A, 464, 1155
Ciotti, L., D'Ercole, A., Pellegrini, S., & Renzini, A. 1991, ApJ, 376, 380
Dickey, J. M., & Lockman, F. J. 1990, ARA&A, 28, 215
Diehl, S., & Statler, T. S. 2006, MNRAS, 368, 497
Diehl, S., & Statler, T. S. 2007, ApJ, 668, 150

Diehl, S., & Statler, T. S. 2008a, ApJ, 680, 897
Diehl, S., & Statler, T. S. 2008b, ApJ, 687, 986
Dunn, R. J. H., Allen, S. W., Taylor, G. B., et al. 2010, MNRAS, 404, 180
Fabian, A. C. 2012, ARA&A, 50, 455
Finoguenov, A., Davis, D. S., Zimer, M., & Mulchaey, J. S. 2006, ApJ, 646, 143
Forman, W., Jones, C., & Tucker, W. 1985, ApJ, 293, 102
Freeman, P., Doe, S., & Siemiginowska, A. 2001, Proc. SPIE, 4477, 76
Fruscione, A., McDowell, J. C., Allen, G. E., et al. 2006, Proc. SPIE, 6270, 62701V
Gabriel, C., Denby, M., Fyfe, D. J., et al. 2004, in ASP Conf. Ser., 314, Astronomical Data Analysis Software and Systems (ADASS) XIII, ed. F. Ochsenbein, M. G. Allen, & D. Egret (San Francisco, CA: ASP), 759
Giacintucci, S., O'Sullivan, E., Vrtilek, J., et al. 2011, ApJ, 732, 95
Goulding, A. D., Greene, J. E., Ma, C.-P., et al. 2016, ApJ, 826, 167
Grevesse, N., & Sauval, A. J. 1998, SSRv, 85, 161
Ji, J., Irwin, J. A., Athey, A., Bregman, J. N., & Lloyd-Davies, E. J. 2009, ApJ, 696, 2252
Johansson, P. H., Naab, T., & Ostriker, J. P. 2009, ApJL, 697, L38
Jones, C., Forman, W., Vikhlinin, A., et al. 2002, ApJL, 567, L115
Jones, L. R., Ponman, T. J., & Forbes, D. A. 2000, MNRAS, 312, 139
Jones, L. R., Ponman, T. J., Horton, A., et al. 2003, MNRAS, 343, 627
Kawaharada, M., Makishima, K., Kitaguchi, T., et al. 2009, ApJ, 691, 971
Khosroshahi, H. G., Ponman, T. J., & Jones, L. R. 2006, MNRAS, 372, L68
Kim, D.-W., Anderson, C., Burke, D., et al. 2019, ApJS, 241, 36
Kim, D.-W., & Fabbiano, G. 2013, ApJ, 776, 116
Kim, D.-W., & Fabbiano, G. 2015, ApJ, 812, 127
Kim, D.-W., Fabbiano, G., & Pipino, A. 2012, ApJ, 751, 38
Kim, D.-W., & Pellegrini, S. 2012, Hot Interstellar Matter in Elliptical Galaxies (New York: Springer)
Kim, D.-W., Traynor, L., Paggi, A., et al. 2020, MNRAS, 492, 2095
Kirkpatrick, C. C., Gitti, M., Cavagnolo, K. W., et al. 2009, ApJL, 707, L69
Kirkpatrick, C. C., McNamara, B. R., & Cavagnolo, K. W. 2011, ApJL, 731, L23
Kolokythas, K., O'Sullivan, E., Giacintucci, S., et al. 2020, MNRAS, 496, 1471
Lakhchaura, K., Werner, N., Sun, M., et al. 2018, MNRAS, 481, 4472
McNamara, B. R., Russell, H. R., Nulsen, P. E. J., et al. 2016, ApJ, 830, 79
Nevalainen, J., Markevitch, M., & Lumb, D. 2005, ApJ, 629, 172
O'Sullivan, E., David, L. P., & Vrtilek, J. M. 2014, MNRAS, 437, 730
O'Sullivan, E., Ponman, T. J., & Collins, R. S. 2003, MNRAS, 340, 1375
O'Sullivan, E., Vrtilek, J. M., & Kempner, J. C. 2005, ApJL, 624, L77
Paggi, A., Kim, D.-W., Anderson, C., et al. 2017, ApJ, 844, 5
Panagoulia, E. K., Sanders, J. S., & Fabian, A. C. 2015, MNRAS, 447, 417
Rasmussen, J., & Ponman, T. J. 2009, MNRAS, 399, 239
Sanders, J. S. 2006, MNRAS, 371, 829
Sato, K., Kawaharada, M., Nakazawa, K., et al. 2010, PASJ, 62, 1445
Snowden, S. L., & Kuntz, K. D. 2011, AAS Meeting Abstracts, 217, 344.17
Sun, M., Forman, W., Vikhlinin, A., et al. 2003, ApJ, 598, 250
Sun, M., Voit, G. M., Donahue, M., et al. 2009, ApJ, 693, 1142
Trinchieri, G., Kim, D. W., Fabbiano, G., & Canizares, C. R. C. 1994, ApJ, 428, 555
Vikhlinin, A., Markevitch, M., Murray, S. S., et al. 2005, ApJ, 628, 655
ZuHone, J. A., Kowalik, K., Ohman, E., Lau, E., & Nagai, D. 2018, ApJS, 234, 4